Asian Journal of Pharmaceutical Sciences 19 (2024) 100944

Available online at www.sciencedirect.com

ScienceDirect

journal homepage: www.elsevier.com/locate/AJPS

Research Article

Co-delivery of retinoic acid and miRNA by functional Au nanoparticles for improved survival and CT imaging tracking of MSCs in pulmonary fibrosis therapy

Xiaodi Li[a,b], *Shengnan Cheng*[a,b], *Chenggong Yu*[a], *Yuxuan Li*[a,b], *Xiaoling Cao*[a,b], *Yuhan Wang*[a], *Zhijun Zhang*[a], *Jie Huang*[a,b,*]

[a] *Organoid Innovation Center, CAS Key Laboratory of Nano-Bio Interface, Division of Nanobiomedicine, Suzhou Institute of Nano-Tech and Nano-bionics, Chinese Academy of Sciences, Suzhou 215123, China*

[b] *School of Nano-Tech and Nano-Bionics, University of Science and Technology of China, Hefei 230026, China*

ARTICLE INFO

Article history:
Received 29 December 2023
Revised 9 May 2024
Accepted 18 May 2024
Available online 14 July 2024

Keywords:
CT imaging tracking
Gold nanoparticles
Idiopathic pulmonary fibrosis
Mesenchymal stem cells
Drug delivery

ABSTRACT

Mesenchymal stem cells (MSCs) have emerged as promising candidates for idiopathic pulmonary fibrosis (IPF) therapy. Increasing the MSC survival rate and deepening the understanding of the behavior of transplanted MSCs are of great significance for improving the efficacy of MSC-based IPF treatment. Therefore, dual-functional Au-based nanoparticles (Au@PEG@PEI@TAT NPs, AuPPT) were fabricated by sequential modification of cationic polymer polyetherimide (PEI), polyethylene glycol (PEG), and transactivator of transcription (TAT) penetration peptide on AuNPs, to co-deliver retinoic acid (RA) and microRNA (miRNA) for simultaneously enhancing MSC survive and real-time imaging tracking of MSCs during IPF treatment. AuPPT NPs, with good drug loading and cellular uptake abilities, could efficiently deliver miRNA and RA to protect MSCs from reactive oxygen species and reduce their expression of apoptosis executive protein Caspase 3, thus prolonging the survival time of MSC after transplantation. In the meantime, the intracellular accumulation of AuPPT NPs enhanced the computed tomography imaging contrast of transplanted MSCs, allowing them to be visually tracked *in vivo*. This study establishes an Au-based dual-functional platform for drug delivery and cell imaging tracking, which provides a new strategy for MSC-related IPF therapy.

* Corresponding author.
E-mail address: jhuang2008@sinano.ac.cn (J. Huang).
Peer review under responsibility of Shenyang Pharmaceutical University.

https://doi.org/10.1016/j.ajps.2024.100944

1. Introduction

Idiopathic pulmonary fibrosis (IPF), with characteristics of chronicity, irreversibility, and high fatality, is the most common clinical manifestation of interstitial pneumonia [1]. In recent years, mesenchymal stem cells (MSCs) have shown great potential in IPF treatment due to their abilities of pluripotent differentiation, anti-inflammatory, immunomodulatory and tissue repair [2]. Numerous clinical trials of IPF treatment have demonstrated the efficacy and safety of MSC therapy [3]. However, the effectiveness of MSC therapy is limited, especially its long-term therapeutic effect has not been reflected, which greatly hinders the clinical transformation of MSCs [4]. The main reason is that the harsh environment at injury site leads to the low viability of MSCs after transplantation (more than 80 %−90 % death within 7 d) [5].

Reactive oxygen species (ROS) with high concentration at the site of pulmonary fibrosis is a major factor in the high mortality of transplanted MSCs. The exposure of transplanted MSCs to ROS environment can cause the destruction of their mitochondrial outer membrane, followed by the activation of the downstream apoptosis protein, ultimately resulting in apoptosis, which is referred to as the internal mechanism of apoptosis [6]. Retinoic acid (RA), a bioactive derivative of vitamin A, has been proven to inhibit apoptosis by regulating the expression of intracellular genes [7]. RA is able to reduce the high concentrations of ROS within transplanted MSCs by increasing the activity of intracellular antioxidants, such as superoxide dismutase (SOD) [8]. In addition to the internal mechanism of apoptosis, a high concentration of ROS induces inflammation and subsequently activates the apoptosis executive protein Caspase 3, thus resulting in the occurrence of the external pathway of apoptosis [9]. microRNA (miRNA) is a type of endogenous non-coding regulatory RNA consisting of 19–22 nucleotides that can target specific mRNAs after transcription, causing them to degrade or inhibit translation [10]. As a result, miRNA plays a vital role in regulating various *in vivo* physiological processes such as development, cell differentiation, and apoptosis [11]. Caspase 3 is a key executive protein in the process of external pathway of apoptosis [12]. As reported, let-7b is a miRNA that can decrease the expression of Caspase 3 within cells, thereby reducing apoptosis [13]. Therefore, co-delivery of RA and miRNA (let-7b) into MSCs not only eliminates intracellular ROS, but also inhibits the expression of intracellular apoptosis executive protein Caspase 3, lessening apoptosis caused by internal and external pathways, as a consequence, improving cell survival after transplantation.

Another challenge in advancing the clinical application of MSCs is the lack of clarity regarding their distribution, location, and movement during treatment, which limits our comprehension of the destiny of MSCs in IPF therapy [14]. Therefore, it is necessary to develop appropriate cell imaging methods for real-time and non-invasive monitoring of the behavior of post-transplanted MSCs *in vivo* [15]. Owing to the diminished proton density in lung tissue, computed tomography (CT) imaging technique, characterized by its high temporal-spatial resolution, has proven to be a valuable tool for monitoring MSCs in IPF treatment [16]. To improve the CT imaging contrast of engrafted MSCs *in vivo*, gold nanoparticles (AuNPs) are often employed as CT contrast agents to label MSCs [17], owing to their good biocompatibility [18], strong X-ray attenuation coefficient [19], and controllable surface property [20]. Since CT signal strength correlates positively with the concentration of intracellular AuNPs, as well as the fact that nucleic acid drugs need to be endocytosed to function in MSCs, AuNPs with high cell entry capacity are required for simultaneous stem cell CT imaging and drug delivery. Several studies have shown that the modification of cationic transfection agent polyethylenimine (PEI) can improve the cellular uptake of NPs and promote the endocytosis of negatively charged drugs [21], but the disadvantage of PEI is that it is too toxic [22]. Coupling of polyethylene glycol (PEG) or transactivator of transcription (TAT) penetration peptide on NPs may help reduce the cytotoxicity of PEI [23], and improve the biocompatibility of NPs [24]. Moreover, TAT, as a penetrating peptide [25], can also interact with proteins on cell surface to promote drug delivery of NPs [26].

In order to inhibit apoptosis and monitor the behavior of transplanted MSCs, we herein report excogitation and construction of positively charged Au-based NPs for co-delivery of RA and miRNA (let-7b) and prolonged *in vivo* CT imaging tracing of transplanted MSCs (Scheme 1). In our strategy, AuNPs were modified with cationic polymer PEI (AuPEI) for loading of RA and miRNA, followed by conjugation with PEG (Au@PEI@PEG NPs, AuPP) to improve the biocompatibility of AuPEI. To further increase the delivery efficiency and enhance the intracellular uptake of NPs, TAT was covalently bonded on the surface of AuPP NPs, acquiring Au@PEI@PEG@TAT (AuPPT) NPs. The cationic AuPPT NPs could highly load negatively charged RA and miRNA (AuPPT/RA/RNA NPs) and easily cross cytomembrane, facilitating not only the efficient delivery of RA and miRNA into MSCs for the elimination of high concentration of ROS and downregulation of Caspase 3 expression within cells, but also the intracellular accumulation of NPs for the enhancement of CT imaging contrast of MSCs. After trachea injection of the AuPPT/RA/RNA NPs labeled MSCs into the pulmonary tissue of IPF model mouse, the survival time of MSCs was significantly extended, thus greatly improving the therapeutic effect of IPF. Meanwhile, the behavior of MSCs could be visualized by CT imaging, thereby deepening the comprehending of MSC-based IPF therapy mechanism. Overall, the bifunctional Au-based NPs possess a promising potential in augmenting the efficacy of MSCs and elucidating their mechanism in IPF treatment.

2. Materials and methods

2.1. Synthesis and characterization of AuPPT NPs

Sodium citrate stabilized AuNPs were prepared as described previously [24]. Briefly, $HAuCl_4$ aqueous solution (100 ml, 2.43×10^{-4} M) was boiled under vigorous agitation, and then trisodium citrate solution (1 ml, 1 %) was introduced. The mixture continued to boil for 15 min. Following cooling down to room temperature, the pH of the solution was modified

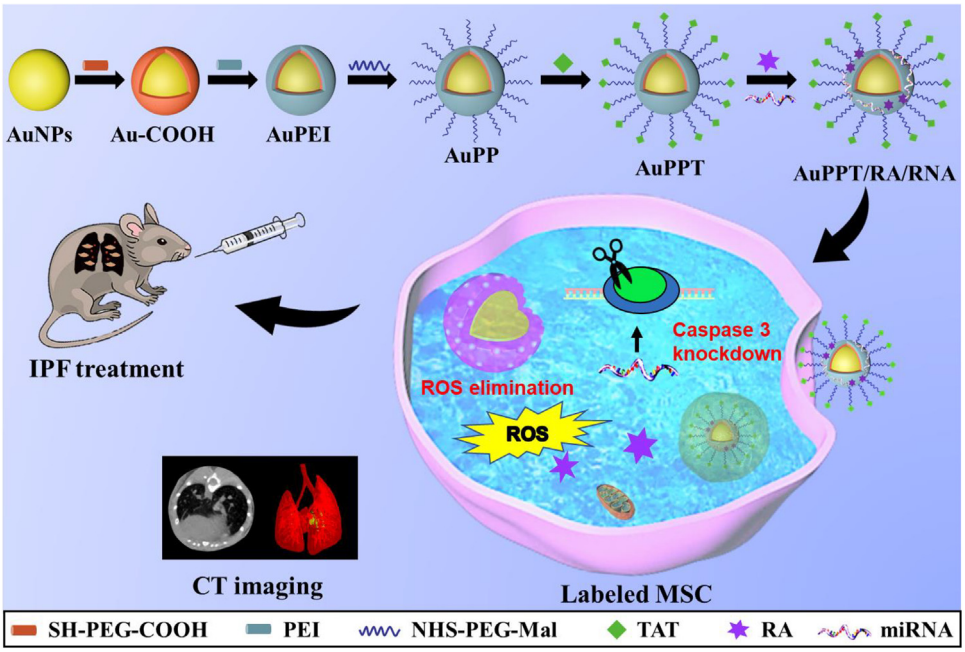

Scheme 1 – Schematic diagram of the preparation of AuPPT/RA/RNA NPs as well as CT imaging tracking and improved therapy of transplanted MSCs labeled with AuPPT/RA/RNA NPs in BLM-induced IPF mouse.

to 11 with NaOH solution (1 M), followed by addition of SH-PEG-COOH (60 mg). After stirring overnight, the product was harvested by centrifugation at 6000 rpm for 10 min and rinsed with ultrapure water twice to remove the unreacted SH-PEG-COOH. The obtained carboxyl modified NPs (Au-COOH) were redispersed in aqueous solution (4.7 mg/ml, 100 ml), and then mixed with 1-ethyl-3-(3-dimethylaminopropyl) carbodiimide (EDC, 2.35 mg) and PEI (2.35 mg) in sequence under stirring for 12 h. After that, NHS-PEG-Mal (14.1 mg) was added to the reaction mixture with stirring for another 12 h to form Au@PEI@PEG (AuPP) NPs, which were then centrifuged at 6000 rpm for 10 min to remove the unreacted materials. For preparation of Au@PEI@PEG@TAT (AuPPT) NPs, TAT (7.05 mg) was added into AuPP NPs colloidal solution (4.7 mg/ml, 100 ml) and stirred for 12 h, followed by centrifuging at 6000 rpm for 10 min to remove unreacted materials.

The morphology of the NPs was examined by transmission electron microscopy (TEM, HT7700, Hitachi). The UV–vis absorption spectra of the intermediate products were detected by UV–vis spectrophotometer (UV–2500, Shimadzu). The hydrodynamic size and zeta potential of various NPs were measured by Malvern particle size meter (ZEN3600-nanoZS, Malvern).

2.2. *miRNA binding and RA loading*

The binding capacity of miRNA on NPs was determined by polyacrylamide gel electrophoresis (PAGE) retardation assay. In brief, miRNA was combined with AuPPT NPs with or without RA loading at various weight ratios of Au to miRNA (1, 2, 4, 8, 12, 24, 48 and 60), and incubated for 30 min to form AuPPT/RNA and AuPPT/RA/RNA NPs. After mixing with 6 × loading buffer (containing GoldView II), PAGE gel electrophoresis was performed using 8 % gel with Tris-Borate-EDTA (TBE, 1 ×) buffer at 110 V for 15 min. Images were obtained on Amersham Imager 600.

For RA loading, RA was first dispersed in dimethyl sulfoxide (DMSO) to prepare a reserve solution (20 mM), which was stocked at −80 °C under dark for future use. Next, AuPPT/RNA NPs colloidal solution (AuPPT/RNA NPs dissolved in 10 mM HEPES buffer, 4.7 mg/ml) was mixed with RA at the different mass ratios of RA to Au (0.1, 0.2, 0.5 and 1). After the mix solution was violently stirred for 3 h, the mixture was centrifuged and then the absorbance value at 350 nm of free RA in the supernatant was recorded by UV–vis absorption spectrometer for calculation of the drug loading content according to the following equation:

$$\text{Drug loading content (\%)} = \frac{W_{RA}}{W_{NPs}} \times 100\%$$

Where, W_{RA} and W_{NPs} denote the weight of RA on NPs and total weight of NPs, respectively.

2.3. *Cytotoxicity of NPs*

AuPPT, AuPEI and AuPP NPs at various concentrations (0, 25, 50, 75 and 100 μg Au/ml) were incubated with MSCs for 24 h, respectively, and the cell viability was detected using cell counting kit 8 (CCK-8) detection kit.

2.4. *miRNA cell transfection assay*

MSCs were planted in 48-well plates (2×10^4 cells per well) and transfected after the cell density reached 60 %–80 %. AuPPT and AuPP NPs (100 μg Au/ml) were respectively incubated with Cy3-taged miRNA (Cy3-miRNA) at different weight ratios

of Au to miRNA (12, 24, 48 and 60) in DMEM high-glucose basic medium (without serum and antibiotics) for 30 min, obtaining AuPPT/RNA and AuPP/RNA. After incubating with AuPPT/RNA or AuPP/RNA NPs for different times (4, 8, 12 and 24 h), the MSCs were observed by confocal laser fluorescence microscopy to study the cell endocytosis of Cy3-miRNA.

To determine the optimal concentration of NPs for cell transfection, different concentrations of AuPPT NPs with or without RA loading were mixed with Cy3-miRNA at a mass ratio of 12 (Au:miRNA) for 30 min, and then incubated with MSCs (2×10^4 cells per well) for 4 h, followed by observation with laser confocal microscopy.

To evaluate whether RA loading affected miRNA transfection by NPs, MSCs (2×10^4 cells per well) were incubated with AuPPT/RNA and AuPPT/RA/RNA (100 μg Au/ml, Au:miRNA=12) for 4 h, respectively. The MSCs treated with free Cy3-miRNA or AuPPT NPs were used as negative control.

2.5. Cytoprotective effects of AuPPT/RA/RNA NPs

MSCs (1×10^4 cells per well) were planted in 96-well plates and cultivated for 24 h. After the cell density reached 80 %, the MSCs were incubated with H_2O_2 solution (diluted in complete medium) at different concentrations (0, 0.2, 0.3, 0.34, 0.38, 0.42, 0.46, 0.5, 0.55, 0.6, 0.7, 0.8, 0.9 and 1 mM) for 12 h, followed by CCK-8 detection, to detect the cell damage. The concentration of H_2O_2 that induced 50 % cell death was employed for the subsequent cytoprotective detection.

To assess the protect effect of AuPPT/RA/RNA NPs on MSCs, MSCs (2×10^4 cells per well) were seeded in 48-well plates and then cultured for 24 h. Subsequently, the MSCs were co-cultured with AuPPT/RA/RNA, AuPPT/RNA or AuPPT/RA NPs (100 μg Au/ml) for 4 h. After washing with phosphate buffered saline (PBS), the labeled MSCs were cultured with 0.34 mM H_2O_2 solution (diluted in complete medium) for 12 h. Cell viability was measured using CCK-8. The cytoprotective effect of AuPPT NPs, RA and miRNA was examined according to the above protocol.

2.6. Cell apoptosis detection

MSCs (3×10^4 cells per well) were planted in 48-well plates and then cultivated for 12 h. After the cells reached 80 % confluence, the MSCs were first incubated with AuPPT/RA/RNA, AuPPT/RNA and AuPPT/RA NPs (100 μg Au/ml) for 4 h, respectively, and then cultured with H_2O_2 solution (0.34 mM, diluted in complete medium) for 12 h. After washing with PBS, Annexin V-FITC binding solution (195 μl) and Annexin V-FITC (5 μl) were added into each well for the detection of phosphatidylserine on the surface of apoptotic MSCs. Following that, propidium iodide (PI) solution (10 μl) was added for the observation of necrotic or late apoptotic cells. Confocal fluorescence microscope was applied for apoptosis detection.

2.7. Intracellular ROS detection

MSCs (3×10^4 cells per well) were planted in 48-well plates and cultured for 12 h. After the cell density reached 80 %, the content of intracellular ROS was tested by ROS detection kit. In brief, the MSCs were incubated with AuPPT/RA/RNA, AuPPT/RNA, and AuPPT/RA NPs (100 μg Au/ml) for 4 h, respectively, followed by incubation with H_2O_2 solution (0.34 mM, diluted in complete medium) for 12 h. After washing with PBS, the MSCs were incubated with 2′,7′-dichlorodihydrofluorescein diacetate (DCFH-DA), a ROS detection probe, for 20 min, and then observed by confocal microscopy.

2.8. Animal experiments

All animal experiments were authorized by Animal Care and Use Committee, Suzhou Institute of Nano-Tech and Nano-Bionics, Chinese Academy of Sciences, and performed under relevant regulations and ethical instructions (Approved number: SINANO/EC/2020–030). The C57BL/6 mice (male, 20–25 g) were injected with bleomycin (BLM) through tracheal administration after anesthesia for IPF animal model construction, according to our established protocol [14]. After 3 d induction, the mice were assigned into 4 groups ($n = 5$ for each group): Control, BLM, AuPPT, and AuPPT/RA/RNA groups. The healthy mice only treated with 50 μl normal saline were used as control group. In BLM group, the IPF mice were administrated with 50 μl normal saline. In the case of AuPPT and AuPPT/RA/RNA groups, the IPF mice were injected with the MSCs labeled with AuPPT or AuPPT/RA/RNA NPs (4×10^6 cells were suspended in PBS for each mouse, total volume of cell suspension was 75 ul for each mouse) through trachea using intubation. After the injection, the mice tilted for about 20 min to ensure a uniform distribution of cells in the lung. To estimate the effect of drug delivery on cell survival, the MSCs (1×10^6 cells) were first incubated with luciferase reporter lentivirus at 1000 virus particle per cell to establish luciferase high-expression MSC cell line. Subsequently, the luciferase-expressing MSCs were incubated with AuPPT or AuPPT/RA/RNA NPs (3 ml, 100 μg Au/ml) for 4 h, followed by injection into IPF mice. [24].

2.9. In vivo CT and bioluminescence (BL) imaging

In vivo micro-CT scanning (Hiscan XM) of the mice in the AuPPT/RA/RNA group was performed at 1, 4, 7, and 11 d after injection of the labeled MSCs. After CT scanning, D-luciferin substrate (150 mg/kg for each mouse) was injected into the abdominal cavity of the anesthetized mice for BL imaging (Caliper Life Science). The BL imaging of the mice in AuPPT group was captured at 1, 2, 3 and 5 d BL and CT images were analyzed using Living Image and Hiscan Analyzer software, respectively.

2.10. Enzyme-linked immunosorbent assay (ELISA)

The lung tissues (0.07–0.1 g) of the mice in each group were added into pre-cooled normal saline at a ratio of 1:9 (m/m) and homogenized with a homogenizer. After centrifugation at 3500 rpm for 20 min at 4 °C, the protein concentrations, including tumor necrosis factor-α (TNF-α), interleukin-6 (IL-6), and interleukin-1β (IL-1β) in the supernatant of the tissue homogenate in each group, were tested with ELISA kit.

2.11. Statistical analysis

All statistical data were presented as mean ± SD and analyzed using GraphPad Prism. Student's t-test and one-way analysis of variance (ANOVA) were used in statistical comparisons of two groups and multiple groups, respectively, and the P-value < 0.05 indicated statistical significance.

3. Results and discussion

3.1. Preparation and characterization of AuPPT NPs

The fabrication of AuPPT NPs is depicted in Scheme 1. Firstly, AuNPs were prepared according to Frens's method [27]. The particles displayed a characteristic plasmon resonance peak at 533 nm, with a hydrodynamic diameter of 38.7 nm and a negative surface charge of −8.4 mV (Fig. 1B-D). Subsequently, AuNPs were coated with SH-PEG-COOH under alkaline condition to form Au-COOH NPs, which had an increased hydrodynamic size of 45.6 nm, and a reduced surface charge of −27.5 mV (Fig. 1C and D). For drug delivery, PEI was covalently bound to Au-COOH NPs through EDC chemistry, producing Au@PEI (AuPEI) NPs. The hydrodynamic diameter of AuPEI was further increased to 48.4 nm, and the surface potential was reversed to 50.1 mV (Fig. 1C and D), which was conducive to the adsorption of negatively charged nucleic acids and chemical drugs. Nevertheless, PEI often causes high cytotoxicity [22]. Hence, NHS-PEG-Mal was modified onto AuPEI NPs through covalent linkage to improve biocompatibility, obtaining Au@PEI@PEG (AuPP) NPs. Compared to AuPEI NPs, the surface charge of AuPP NPs was obviously decreased to 39.8 mV, and their hydrodynamic size continued to increase to 59.4 nm (Fig. 1C and D). However, PEG modification typically reduces the cellular uptake of NPs, impeding the entry of drugs into cells [28]. To address this issue, TAT penetration peptide was further conjugated to the particles through chemical reaction between the sulfhydryl group on TAT peptide and the maleimide on the bonded PEG for the enhancement of cell endocytosis, thereby gaining Au@PEI@PEG@TAT (AuPPT) NPs. TEM image showed that the resulted AuPPT NPs had a spherical morphology with an average particle size of 36.5 nm (Fig. 1A). After TAT grafting, the hydrodynamic size of AuPPT NPs increased to 72.9 nm (Fig. 1C), and the zeta potential slightly increased to 44.6 mV (Fig. 1D), beneficial for drug loading and intracellular delivery. Then, the FT-IR (Fourier transform infrared spectroscopy) spectra of Au-COOH, AuPEI, AuPP, and AuPPT NPs were detected (Fig. S1). In the FT-IR spectrum of Au-COOH, the characteristic peaks representing -CH- bond appeared at 2849 cm^{-1} and 2924 cm^{-1}, indicating that SH-PEG-COOH was covalently coupled on the surface of Au. After PEI modification, the stretching bond of -C-N- (1319 cm^{-1}) originating from the secondary acid amide was observed, suggesting the covalent linkage between Au-COOH and PEI. In addition to the -C-N- from secondary acid amide, -C=C- (1680 cm^{-1}) and -C=O- (1712 cm^{-1}) bonds belonging to maleimide appeared in the FT-IR spectrum of AuPP NPs, illustrating that the NPs were successfully functionalized by NHS-PEG-Mal. In the FT-IR spectrum of AuPPT NPs, a new characteristic peak was found at 842 cm^{-1}, which was attributed to -C-S- [29]. These results confirmed the successful synthesis of Au-COOH, Au-PEI, AuPP, and AuPPT NPs. During the synthesis process, the UV–Vis absorption characteristic peaks of various NPs remained at about 533 nm, indicative of the stability of these NPs (Fig. 1B). Moreover, the hydrodynamic size and zeta potential of AuPPT NPs had no obvious change within 7 d, further indicating their good stability (Fig. S2).

AuPEI NPs at 75 μg Au/ml caused 20 % cell death after incubating for 24 h, but the cell mortality was decreased to 5 % after PEG modification (AuPP NPs) (Fig. 1E). Significantly, almost no cytotoxicity of AuPPT NPs was detected, even the concentration of Au was increased to 100 μg Au/ml, indicating that the modification of PEG and TAT improved the biocompatibility of particles (Fig. 1E). In order to evaluate the CT imaging performance of AuPPT NPs, CT images and Hounsfield unit (HU) value of AuPPT NPs at different concentrations were detected. The CT images of AuPPT NPs brightened with the increase in Au concentration, and the HU value exhibited a linear correlation with Au concentration, suggesting the exceptional CT imaging ability of AuPPT NPs (Fig. 1F).

3.2. Drug loading and cell labeling of NPs

Individual miRNA is not only difficult to enter into cells, but also easy to be degraded by enzymes in cells, hence, an effective delivery system is needed to deliver miRNA into cytoplasm, as well as protect miRNA from degradation by endogenous enzymes, thus transfecting MSCs [30]. To assess the effectiveness of AuPPT NPs for MSC transfection, AuPPT NPs were mixed with Cy3-miRNA (miRNA tagged with Cy3) at different mass ratios of Au to miRNA (0, 1, 2, 4, 8, 12, 24, 48 and 60) to form a series of AuPPT/RNA NPs. PAGE retardation assay showed complete absorption at a mass ratio of 12 (Au:miRNA) (Fig. 2A, bottom image). Then, MSCs were incubated with AuPPT/RNA NPs (Au:miRNA=12, 24, 48 and 60) for different time points (4, 8, 12 and 24 h) without serum culture, followed by fluorescence confocal microscopy observation to detect the transfection efficiency of miRNA. Fig. S3 shows that the transfection efficiency of Cy3-miRNA at the mass ratios of Au to miRNA more than 24 was lower than that at the mass ratio of 12, probably caused by the low absorption mass of miRNA on NPs. Moreover, the transfection efficiency decreased with the incubation time, likely due to the poor cell viability caused by the lack of serum, thus resulting in reduced endocytosis. To examine the effect of TAT modification on MSC transfection, MSCs were cultured with AuPP/RNA NPs (Au:miRNA=12, 24, 48 and 60) for different time points (4, 8, 12, and 24 h) without serum culture. Similarly, obvious red fluorescence in the MSCs was observed after incubation, but the highest transfection efficiency of AuPP NPs was achieved when the mass ratio of Au to miRNA was 24 after 4 h incubation (Fig. S4). Furthermore, quantitative data demonstrated that the maximum mean fluorescence intensity (MFI) of the MSCs was obtained after incubating with AuPPT/RNA NPs for 4 h at a mass ratio of 12 (Au:miRNA), revealing that the modification of TAT largely improved the nucleic acid transfection ability of the Au-

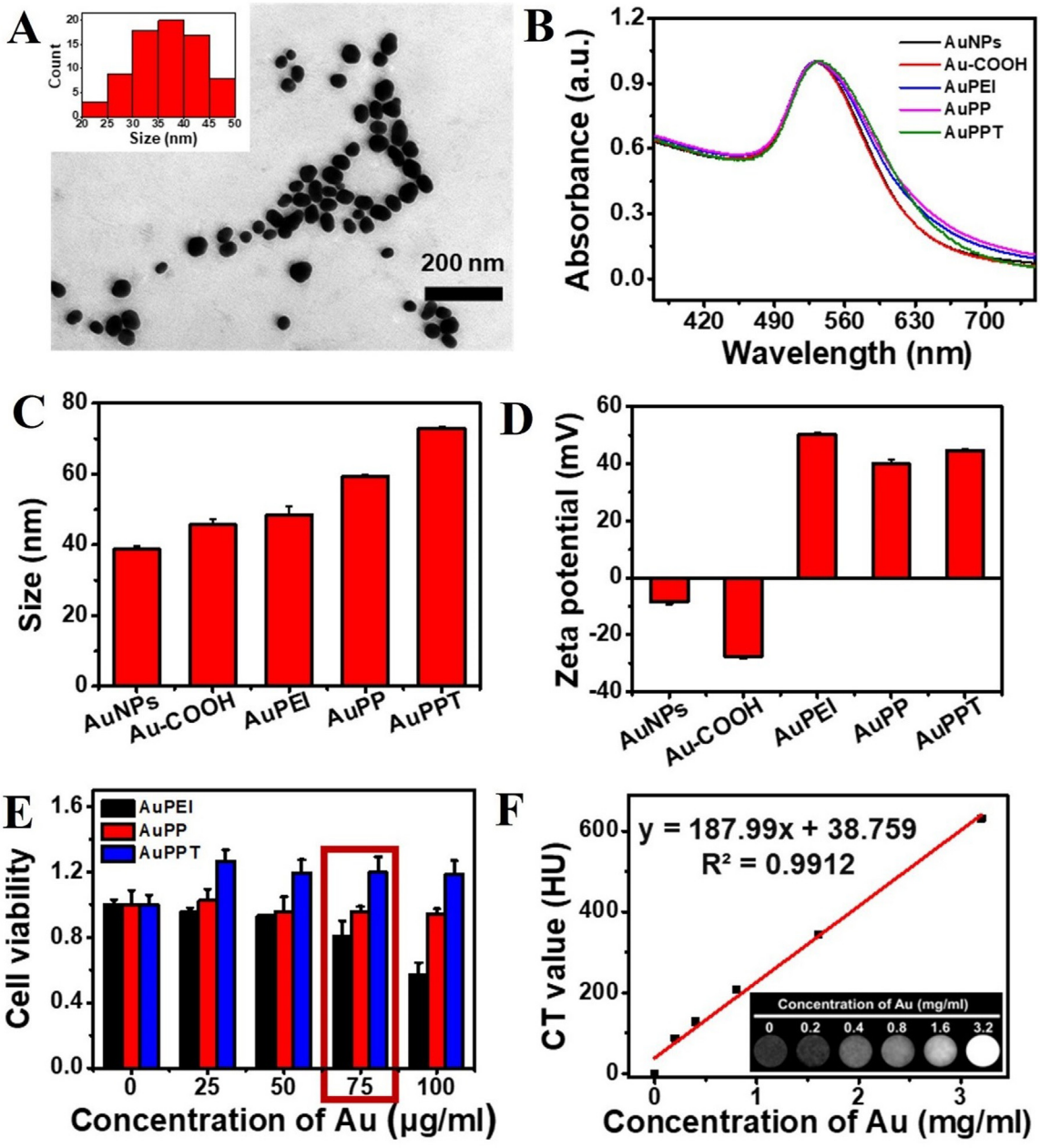

Fig. 1 – (A) TEM image of AuPPT NPs (inset shows the size distribution). (B) UV–vis absorption spectra, (C) hydrodynamic size and (D) zeta potential of AuNPs, Au-COOH, AuPEI, AuPP, and AuPPT NPs. Mean ± SD, *n* = 3. (E) Cell viability of MSCs after labeling with AuPEI, AuPP, or AuPPT NPs at different concentrations within 24 h. Mean ± SD, *n* = 4. (F) CT images of AuPPT NPs with different concentrations and the linear relation of HU value and Au concentration.

based NPs (Fig. S5). The extraordinary transfection efficiency of AuPPT NPs may be attributed to PEI, a cationic polymer with high transfection capacity. On the other hand, the interaction between TAT and cell membrane proteins (such as clathrin and concave proteins) further promoted the endocytosis of AuPPT NPs [31]. Therefore, MSCs incubated with AuPPT/RNA NPs at the mass ratio of 12 (Au:miRNA) for 4 h was selected as delivery condition for subsequent experiments.

In order to clear the intracellular high concentration of ROS, RA was loaded onto AuPPT/RNA NPs (Au:miRNA=12) by electrostatic adsorption, obtaining AuPPT/RA/RNA NPs. For optimal loading capacity, AuPPT/RNA NPs and RA were mixed at different mass ratios of RA to Au (0.1, 0.2, 0.5 and 1) in HEPES buffer solution. AuPPT/RA/RNA NPs at the mass ratios of 0.5 or 1 (RA:Au) aggregated severely in buffer solution, the hydrodynamic size reached 170 nm and the polymer dispersity index (PDI) value exceeded 0.5 (Table S1). While, when the mass ratios of RA to Au were 0.2 and 0.1, AuPPT/RA/RNA NPs presented good dispersion (PDI=0.293 and 0.269, respectively) and relatively small hydrodynamic size of 74.6 and 72.8 nm, respectively. Hence, in this study, AuPPT/RA/RNA NPs at the mass ratio of 0.2 (RA:Au) was

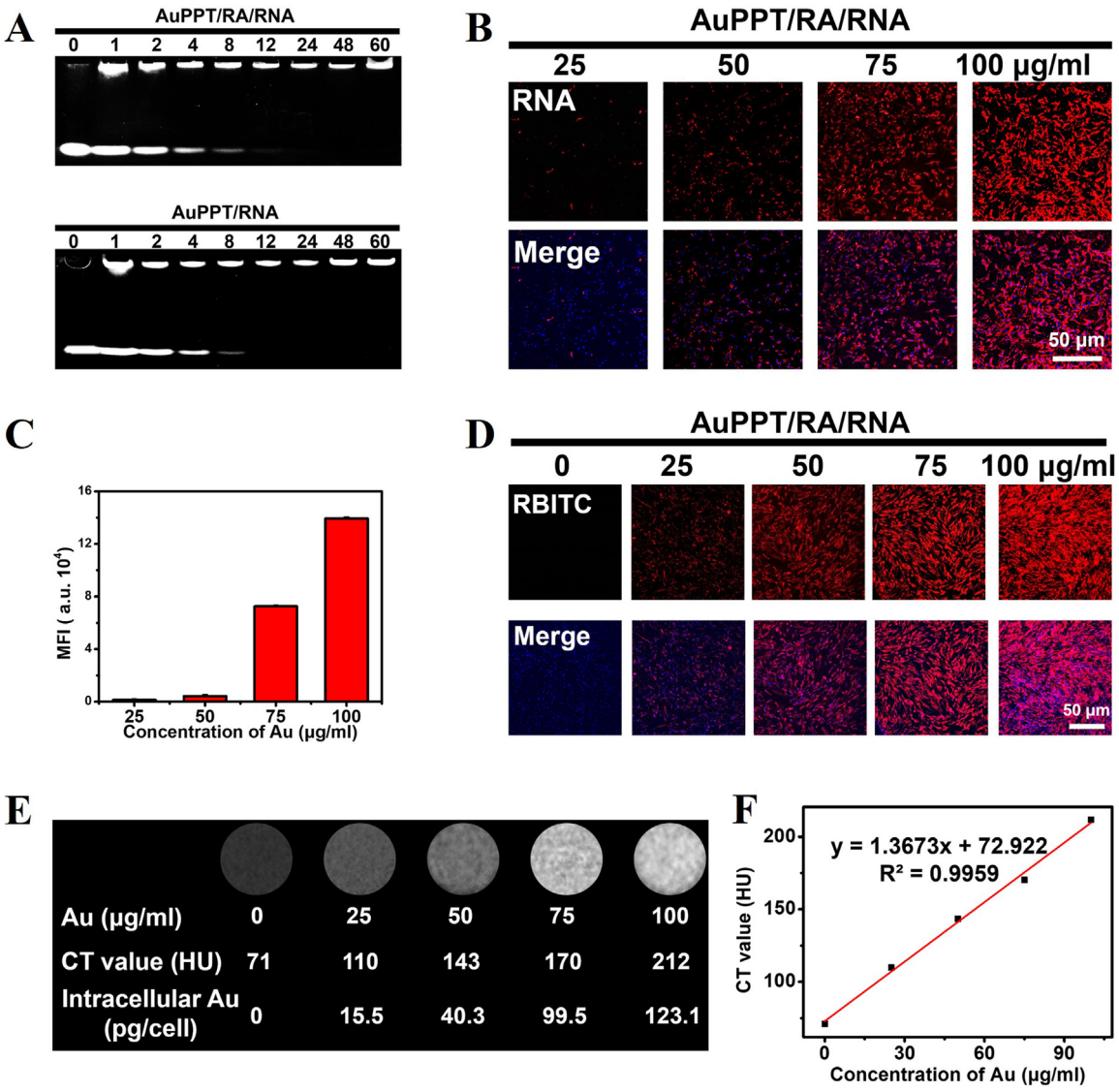

Fig. 2 – (A) PAGE retardation assay of AuPPT/RNA and AuPPT/RA/RNA NPs (RA:Au=0.2) at various mass ratios (0, 1, 2, 4, 8, 12, 24, 48, and 60) of Au to miRNA, complete retardation of miRNA was realized at the mass ratio of 12 of Au to miRNA. (B) Confocal laser fluorescence microscopy and (C) MFI of MSCs incubated with AuPPT/RA/RNA NPs (Au:miRNA=12, RA:Au=0.2) for 4 h at various Au concentrations (25, 50, 75 and 100 μg /ml), miRNA was pre-tagged with Cy3 (red), nuclei were stained with DAPI (blue), RNA represented miRNA that was delivered into MSCs. Mean ± SD, *n* = 3. (D) Confocal laser fluorescence microscopy of MSCs incubated with RBITC-AuPPT/RA/RNA NPs at different Au concentrations (0, 25, 50, 75, and 100 μg/ml) for 4 h, the nuclei and NPs were stained by DAPI (blue) and RBITC (red), respectively. (E) CT images of MSCs labeled with AuPPT/RA/RNA at Au concentrations of 0, 25, 50, 75, and 100 μg/ml. (F) Linear fitting diagram of HU values of labeled MSCs relative to Au concentration.

selected for follow-up experiments because of their higher drug encapsulation content (6.24 %).

To examine the effect of RA load on the binding of miRNA to the NPs, the miRNA condensation capability of AuPPT/RA/RNA NPs (RA:Au=0.2) was tested by PAGE retardation assays at different weight ratios of Au to miRNA (0, 1, 2, 4, 8, 12, 24, 48 and 60) (Fig. 2A, top image). Complete absorption of miRNA for AuPPT/RA/RNA NPs was found at the ratio of 12 (Au:miRNA), in good agreement with the result of AuPPT/RNA NPs, declaring that RA loading did not influence the ability of the NPs to bind nucleic acid. The particle size, zeta potential, and TEM image of AuPPT/RA/RNA NPs are provided in Fig. S6. The hydrodynamic size of AuPPT/RA/RNA NPs was measured to be 82.5 nm, higher than that of AuPPT NPs (72.9 nm), resulting from the loading of RA and miRNA. The zeta potential of AuPPT/RA/RNA NPs was about 18.5 mV, much lower than that of AuPPT NPs (44.6 mV), mainly due to the loading of negatively charged RA and miRNA. From the TEM image, AuPPT/RA/RNA NPs still maintained good dispersion after drug loading.

To evaluate the influence of incubating concentration on transfection efficiency, AuPPT/RA/RNA NPs (Au:miRNA=12,

RA:Au=0.2) at different Au concentrations (25, 50, 75 and 100 μg/ml) were incubated with MSCs for 4 h. The results observed by fluorescence microscopy presented that the MFI of MSCs increased with the increase of culture concentration; therefore, the highest transfection efficiency was achieved at 100 μg Au/ml of AuPPT/RA/RNA NPs, which was also verified by quantitative data (Fig. 2B and C), consistent with the transfection result of AuPPT/RNA NPs at various Au concentrations (Fig. S7). Following that, MSCs were incubated with AuPPT/RA/RNA NPs at 100 μg Au/ml for 4 h and observed by fluorescence confocal microscopy to estimate the effect of RA loading on transfection efficiency of miRNA. The MSCs cultured with AuPPT/RNA NPs (100 μg Au/ml, Au:miRNA=12) were served as control. The MSCs only incubated with AuPPT NPs or free miRNA were set as negative control groups. The results showed that the transfection efficiency of AuPPT/RA/RNA was similar to that of AuPPT/RNA NPs, which was also confirmed by quantitative experiments, demonstrating that RA loading did not affect the transfection ability of AuPPT/RA/RNA NPs to MSCs (Fig. S8). It is noteworthy that only a very small amount of free miRNA was transfected into MSCs in the absence of AuPPT delivery (RNA group), confirming the necessity of AuPPT NPs for effective nucleic acid delivery. In short, with the help of PEI and TAT, AuPPT NPs efficiently loaded and delivered miRNA and RA into MSCs.

To assess the cell labeling efficiency of AuPPT/RA/RNA NPs, Rhodamine B isothiocyanate (RBITC) tagged AuPPT/RA/RNA (RBITC-AuPPT/RA/RNA) NPs were co-incubated with MSCs at different concentrations (25, 50, 75 and 100 μg Au/ml) for 4 h, followed by fluorescence microscopy detection and CT scanning. As exhibited in Fig. 2D, significant red fluorescence was observed in the MSCs after culture with RBITC-AuPPT/RA/RNA even at a low incubation concentration (25 μg Au/ml), demonstrating the high labeling efficiency of RBITC-AuPPT/RA/RNA NPs on MSCs. The fluorescence intensity enhanced with the increment of incubation concentration and reached the maximum fluorescence intensity when the labeling concentration was 100 μg Au/ml. Fig. 2E showcases that CT images of the labeled MSCs gradually brightened with the augment of culture concentration, and their CT value was linearly correlated with the Au concentration (Fig. 2F). The maximum CT value and brightest CT images were also obtained at the concentration of 100 μg Au/ml, and the intracellular Au content reached 123.1 pg/cell under this incubating condition, far exceeding the minimum intracellular Au concentration (34 pg/cell) required for *in vivo* CT imaging tracking [32]. Therefore, the labeling condition of 100 μg Au/ml for 4 h was used in subsequent experiments. Taken together, AuPPT NPs were effective not only for drug delivering, but also for cell labeling, which was beneficial for cell protection and *in vivo* CT imaging to be discussed below.

3.3. *Biocompatibility of AuPPT/RA/RNA NPs*

To evaluate whether the AuPPT/RA/RNA labeling affected the propagation and differentiation of stem cells, MSCs were incubated with AuPPT/RA/RNA NPs (100 μg Au/ml) for 4 h, and underwent CCK-8 detection, as well as adipogenic and osteogenic differentiation culture, respectively. The result of 7-d proliferation showed that the labeled MSCs had the same proliferation behavior as the unlabeled MSCs (Fig. S9). In addition, no obvious difference was observed between the MSCs with and without AuPPT/RA/RNA labeling after osteogenic and adipogenic differentiation culture, respectively, followed by Oil Red O and Alizarin Red S staining, unveiling that AuPPT/RA/RNA labeling did not affect the production of lipid droplet and calcium nodules (Fig. 3A and C). The quantitative results further verified that there was no notable difference between the labeled and unlabeled MSCs through measuring the optical density of the extracted Oil Red O and Alizarin Red S at 490 nm and 550 nm, respectively (Fig. 3B and D). The data of proliferation and differentiation demonstrated that AuPPT/RA/RNA NPs possessed good biocompatibility and biosafety, which could be used for *in vivo* experiment.

3.4. *Cell protection of AuPPT/RA/RNA NPs*

The high concentration of ROS of pulmonary fibrosis site can result in the death of grafted stem cells, thus affecting the therapeutic efficacy. In order to verify whether RA and miRNA delivery could improve cell viability under oxidative stress, MSCs were co-incubated with H_2O_2 solution at various concentrations (0, 0.2, 0.3, 0.34, 0.38, 0.42, 0.46, 0.5, 0.55, 0.6, 0.7, 0.8, 0.9 and 1 mM) to construct a cell model of oxidative damage. The cell survival rate was determined to be 49 % when the concentration of H_2O_2 was 0.34 mM, which was used as the cell damage concentration for subsequent experiments (Fig. S10). After incubation with AuPPT/RA, AuPPT/RNA, or AuPPT/RA/RNA NPs (100 μg Au/ml) for 4 h, the labeled MSCs were cultured with 0.34 mM H_2O_2 for 12 h for damage. The MSCs without any treatment and only treated with H_2O_2 were taken as control and H_2O_2 damage groups, respectively. The result showed that the cell survival rate was only 57 % in the H_2O_2 damaged group, significantly lower than that of the control group. However, 67 % and 66 % cells survived in the AuPPT/RA and AuPPT/RNA groups, respectively, showing obvious enhancement compared with the H_2O_2-damaged group. Interestingly, the cell viability increased to 78 % after the addition of AuPPT/RA/RNA NPs, much higher than that of the AuPPT/RA and AuPPT/RNA groups, suggesting that the co-delivery of RA and miRNA had the best cell protection effect (Fig. 4A). It is found that in contrast with the H_2O_2 injury group, early apoptotic and necrotic cells, stained by Annexin V and PI, respectively, were significantly decreased in the AuPPT/RA and AuPPT/RNA groups. Moreover, miRNA and RA co-delivery group (AuPPT/RA/RNA group) showed the lowest cell death, indicating the combined delivery of miRNA and RA increased the viability of MSCs under oxidative stress (Fig. 4B). Subsequently, MSCs were incubated with free AuPPT NPs, miRNA, and RA for 4 h, respectively, and then damaged by H_2O_2 (0.34 mM). No improved cell viability was measured in comparison with the H_2O_2 damage group, indicating that not only AuPPT, but also free miRNA and RA had no protective effects on the damaged cells (Fig. 4C). This phenomenon was mainly due to the difficulty of free miRNA and RA entering into cells. These results confirmed that RA and miRNA were successfully delivered into cells by AuPPT NPs to protect MSCs from H_2O_2 damage, and the combination of the two drugs enhanced the protective effect.

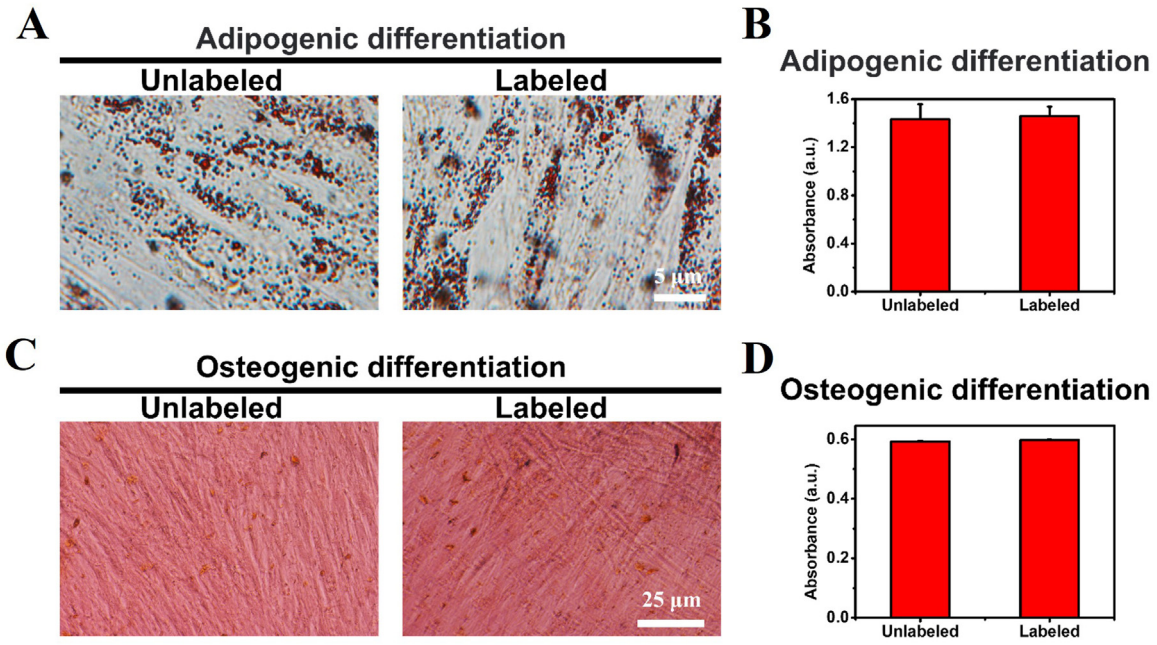

Fig. 3 – (A) Oil Red O staining and (B) quantitative measurement of adipocyte differentiation of MSCs with or without AuPPT/RA/RNA treatment. Mean ± SD, $n = 4$. (C) Alizarin Red S and (D) quantitative measurement of osteoblast differentiation of MSCs with or without AuPPT/RA/RNA treatment. Mean ± SD, $n = 4$.

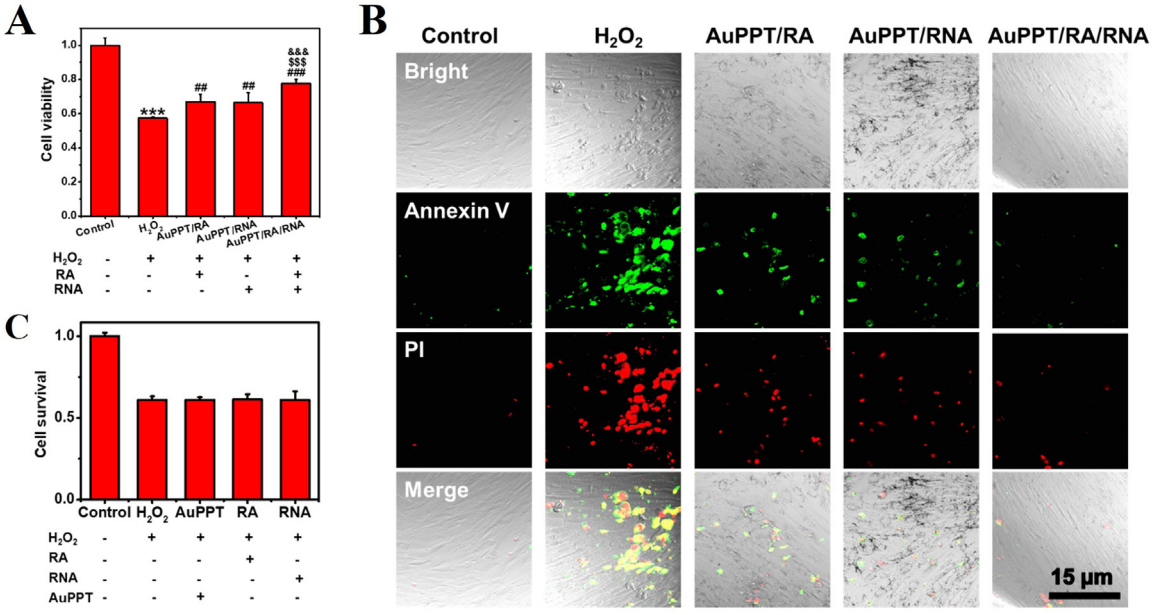

Fig. 4 – (A) Cell viability of MSCs labeled with AuPPT/RA, AuPPT/RNA, or AuPPT/RA/RNA after H_2O_2 damage, the MSCs without any treatment and only treated with H_2O_2 were taken as control and H_2O_2 damage groups, respectively. $^{***}P < 0.001$ compared with control group. $^{\#\#}P < 0.01$ compared with H_2O_2 group. $^{\#\#\#}P < 0.001$ compared with H_2O_2 group. $^{\$\$\$}P < 0.001$ compared with AuPPT/RA group. $^{\&\&\&}P < 0.001$ compared with AuPPT/RNA group. Mean ± SD, $n = 4$. (B) Apoptosis detection of MSCs using Annexin V (green) and PI (red) staining in different groups (Control, H_2O_2, AuPPT/RA, AuPPT/RNA, and AuPPT/RA/RNA) by confocal laser microscopy. (C) Cell survival of MSCs labeled with AuPPT, RA or miRNA after H_2O_2 damage, the MSCs without any treatment and only treated with H_2O_2 were taken as control and H_2O_2 damage groups, respectively. Mean ± SD, $n = 4$.

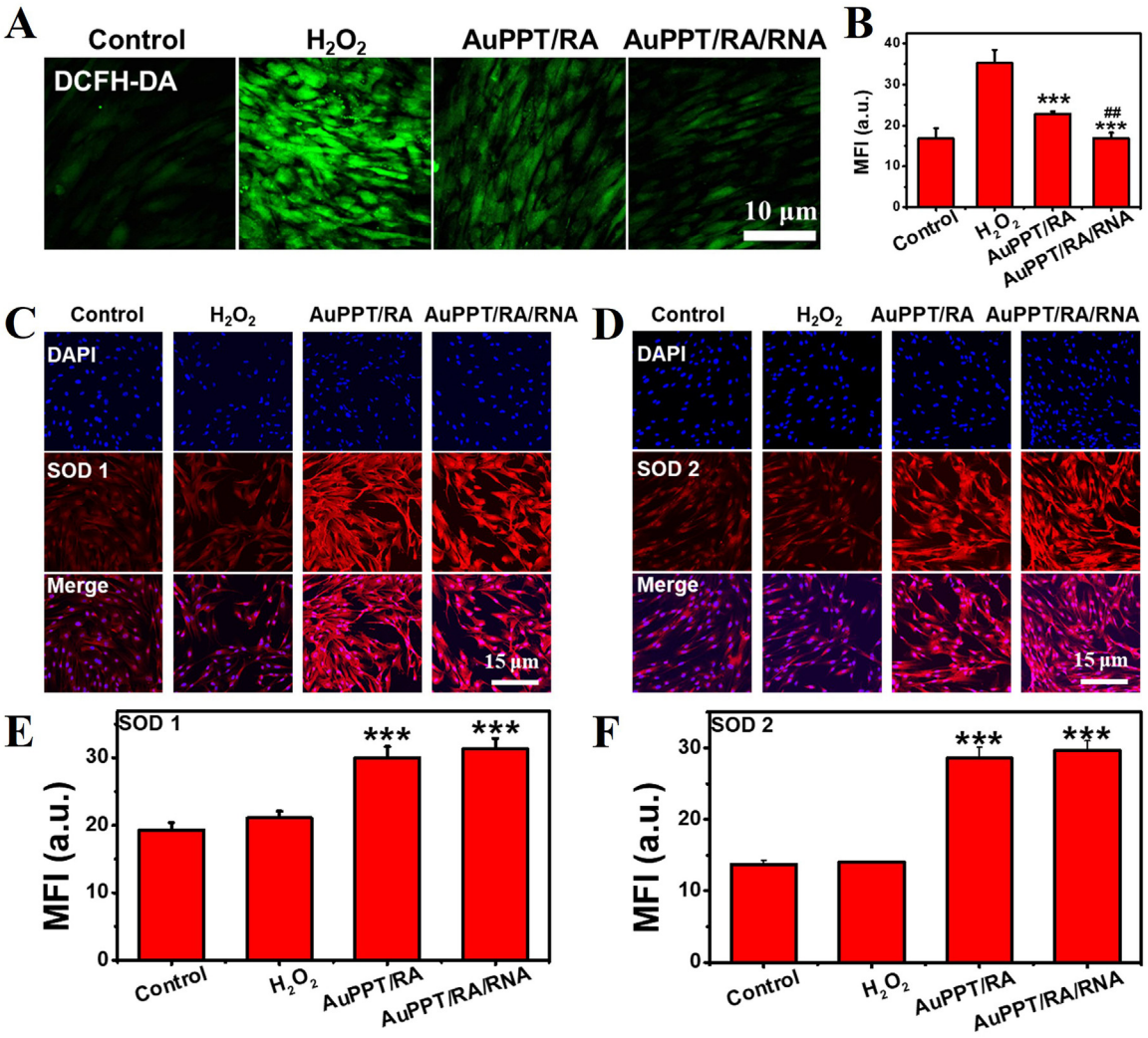

Fig. 5 – (A) Laser confocal microscope images of MSCs stained by DCFH-DA in different groups and (B) corresponding fluorescence intensity, ***$P < 0.001$ compared with H_2O_2 group, $^{\#\#}P < 0.01$ compared with AuPPT/RA group. Mean ± SD, $n = 3$. Representative immunostaining images of (C) SOD 1 (red) and (D) SOD 2 (red) of MSCs in different groups, the nuclei were stained by DAPI (blue). Quantification of fluorescence of (E) SOD 1 and (F) SOD 2 in different groups, ***$P < 0.001$ compared with H_2O_2 group. Mean ± SD, $n = 3$.

3.5. *Mechanism of AuPPT/RA/RNA NPs for cell protection*

RA is a bioactive metabolite of vitamin A with multiple biological functions, including regulation of cell multiplication, apoptosis, and development [33]. It has been reported that RA inhibited the production of ROS in cells by increasing the expression level of intracellular SOD, thereby hindering cell apoptosis and promoting cell survival [34]. To investigate the scavenging mechanism of RA on ROS, MSCs were incubated with AuPPT/RA or AuPPT/RA/RNA NPs (100 μg Au/ml), and then damaged by H_2O_2. The MSCs without any treatment and only treated with H_2O_2 were set as control and H_2O_2 damage groups, respectively. The ROS levels within the MSCs were detected using DCFH-DA probe, which can be oxidized to fluorescent 2′,7′-dichlorofluorescein (DCF) by ROS. Obvious green fluorescence was observed in the MSCs after H_2O_2 damage, indicating a relatively high concentration of ROS within the MSCs (Fig. 5A). Whereas, after the addition of the NPs (AuPPT/RA or AuPPT/RA/RNA), the intracellular green fluorescence decreased significantly, suggestive of a declined ROS level. The quantitative fluorescence intensity showed that the MFI of the AuPPT/RA and AuPPT/RA/RNA groups was markedly lower than that of the H_2O_2-damaged group, in agreement with the results of fluorescence images. It is worth noting that the MFI of the AuPPT/RA/RNA group was lower than that of the AuPPT/RA, which might be explained by the fact that the downregulation of caspase 3 expression by miRNA reduced the endogenous ROS generation (Fig. 5B) [35]. To further verify whether the antioxidant effect of RA is attributable to the regulation of intracellular SOD expression levels, the expression of two subtypes of SOD enzymes, namely cytoplasmic Cu-, Zn-SOD (SOD 1) and mitochondrial Mn-SOD (SOD 2) proteins [34], was studied through immunofluorescence staining. The results showed that the intracellular red fluorescence (SOD 1 enzyme) was significantly enhanced in the AuPPT/RA and AuPPT/RA/RNA

NPs groups compared with the control and H_2O_2 injury groups, indicating that the SOD 1 expression was increased after the addition of the drug-loaded NPs, which were also verified by quantitative experiments (Fig. 5C and E). Similarly, the expression level of SOD 2 (red fluorescence) was also upregulated by AuPPT/RA and AuPPT/RA/RNA NPs, as shown in Fig. 5D and F. Collectively, RA, delivered by AuPPT NPs, elevated the level of intracellular antioxidant SOD, thereby improving the ability of the transplanted MSCs to withstand high concentration of ROS, as a consequence, reducing apoptosis of the MSCs after transplantation.

Abundant studies have substantiated that the expression level of apoptosis-related protein Caspase 3 is increased through external pathways during apoptosis [36]. While, miRNA has been proven to downregulate the expression level of intracellular Caspase 3, inhibiting MSC apoptosis [13]. To test the intracellular expression of Caspase 3 after miRNA delivery, MSCs were first incubated with AuPPT/RNA or AuPPT/RA/RNA NPs (100 μg Au/ml), and then damaged by H_2O_2, followed by immunofluorescence staining to detect the expression level of Caspase 3 within MSCs. The MSCs without any treatment and only treated with H_2O_2 were set as control and H_2O_2 group, respectively. In contrast with the control group, an increased expression level of Caspase 3 (red fluorescence) was clearly observed in the H_2O_2 injury group (Fig. 6A). Of special note, the red fluorescence intensity in the MSCs pre-treated with AuPPT/RNA or AuPPT/RA/RNA was greatly weakened. This phenomenon was also supported by the quantification data, in which the MFI in both AuPPT/RNA and AuPPT/RA/RNA groups was visibly lessened compared to that in the H_2O_2 group, and showed a similar intensity as the control group (Fig. 6B). It is therefore concluded that miRNA delivered by AuPPT NPs inhibited the expression of the intracellular Caspase 3 in the H_2O_2 damaged MSCs. Besides, no significant difference in the expression level of Caspase 3 was seen between the AuPPT/RNA and AuPPT/RA/RNA groups, suggesting that miRNA rather than RA curtailed the intracellular Caspase 3 expression.

Autophagy is an intracellular degradation pathway in which damaged, denatured or senescent proteins and organelles form autophagosomes, which are eliminated through lysosomal digestion and degradation [13]. Under physiological conditions, cells achieve self-protection by degrading damaged organelles and proteins via autophagy, while under pathological conditions such as excessive oxidative stress, immoderate autophagy causes the degradation of normal proteins and organelles, resulting in organ dysfunction and cell death [37]. Thus, the expression of Beclin 1 (BECN 1), a signature protein in the initiation stage of autophagy, and light chain 3B (LC-3B), a protein marker of autophagosome formation, were detected [38]. Compared with the H_2O_2 injured group, the expression levels of BECN 1 and LC-3B in the AuPPT/RNA and AuPPT/RA/RNA groups were largely down-regulated, as evidenced by immunofluorescence staining and corresponding quantitative statistic (Fig. 6C-F). Likewise, no noticeable difference in the MFI of BECN 1 and LC-3B was found between the AuPPT/RNA and AuPPT/RA/RNA groups, revealing that miRNA played an important role in the inhibition of autophagy. As reported, the expression of intracellular apoptosis proteins can affect the expression of autophagy proteins [39]. These results could be explained as: miRNA transfection retarded the ROS-induced increase in autophagy-related protein expression, which may be attributed to the downregulation of apoptosis-related protein Caspase 3 [39]. Therefore, the delivery of miRNA into MSCs by AuPPT NPs restrained the expression of apoptosis- and autophagy-associated proteins.

Taken together, AuPPT/RA/RNA exhibited optimal cell protection, because RA and miRNA co-delivery simultaneously decreased intracellular ROS concentration and inhibited apoptotic protein production, resulting in an improvement of MSC viability under oxidative stress environment.

3.6. *BL and CT imaging tracking of the transplanted MSCs in vivo*

In order to explore the distribution, migration, and location of MSCs after transplantation, the AuPPT/RA/RNA labeled MSCs were injected intratracheally into BLM-induced IPF mice for CT imaging. A noticeable CT signal (red dashed circle) at axial and coronal positions was observed in the lung tissue of the IPF mice after the transplantation of the labeled MSCs, and the CT signals could be continuously detected and monitored for 11 d (Fig. 7A). The 3D reconstruction results of CT imaging exhibited that the transplanted MSCs were mainly distributed in the right lung, and the CT signal volume and value increased steadily with the transplantation time, both reaching the maximum on Day 7 (1.02 mm^3 for CT signal volume, and 170.24 HU for CT signal value), which may be caused by the gradual migration and accumulation of the MSCs in the injury tissue (Fig. 7B-D). Subsequently, the CT signal gradually weakened (from Day 7 to Day 11), likely due to the metabolism and elimination of the dead MSCs by the abundant blood flow at lung site. In a word, AuPPT/RA/RNA NPs labeling combined with CT imaging achieved noninvasive tracking of the migration and distribution of stem cells *in vivo*, which was beneficial to understanding the mechanism of stem cell therapy and promoting the clinical translation of MSCs in the future.

To validate whether RA and miRNA delivery could improve the survival rate of transplanted MSCs, BL imaging was performed on the IPF mice transplanted with the AuPPT/RA/RNA labeled MSCs (AuPPT/RA/RNA group). The IPF mice injected with the AuPPT-labeled MSCs (AuPPT group) acted as control. As displayed in Fig. 7E, strong BL imaging signal representing living cells was observed in the lung tissue of the AuPPT and AuPPT/RA/RNA groups. The BL imaging signals from the AuPPT/RA/RNA group could be detected for 11 d, while the signals in the AuPPT group only maintained for 5 d (Fig. 7E). Furthermore, quantitative results in Fig. 7F showed that the BL signal intensity in both AuPPT and AuPPT/RA/RNA groups increased first and then decreased after cell transplantation *in vivo*, consistent with the results of CT imaging. At the beginning of transplantation, MSCs gradually migrated to the injured site due to their homing ability, resulting in the enhancement of the BL signal intensity. After that, with the death of the transplanted stem cells, the BL imaging signal attenuated little by little. However, in the AuPPT group, the BL signals displayed

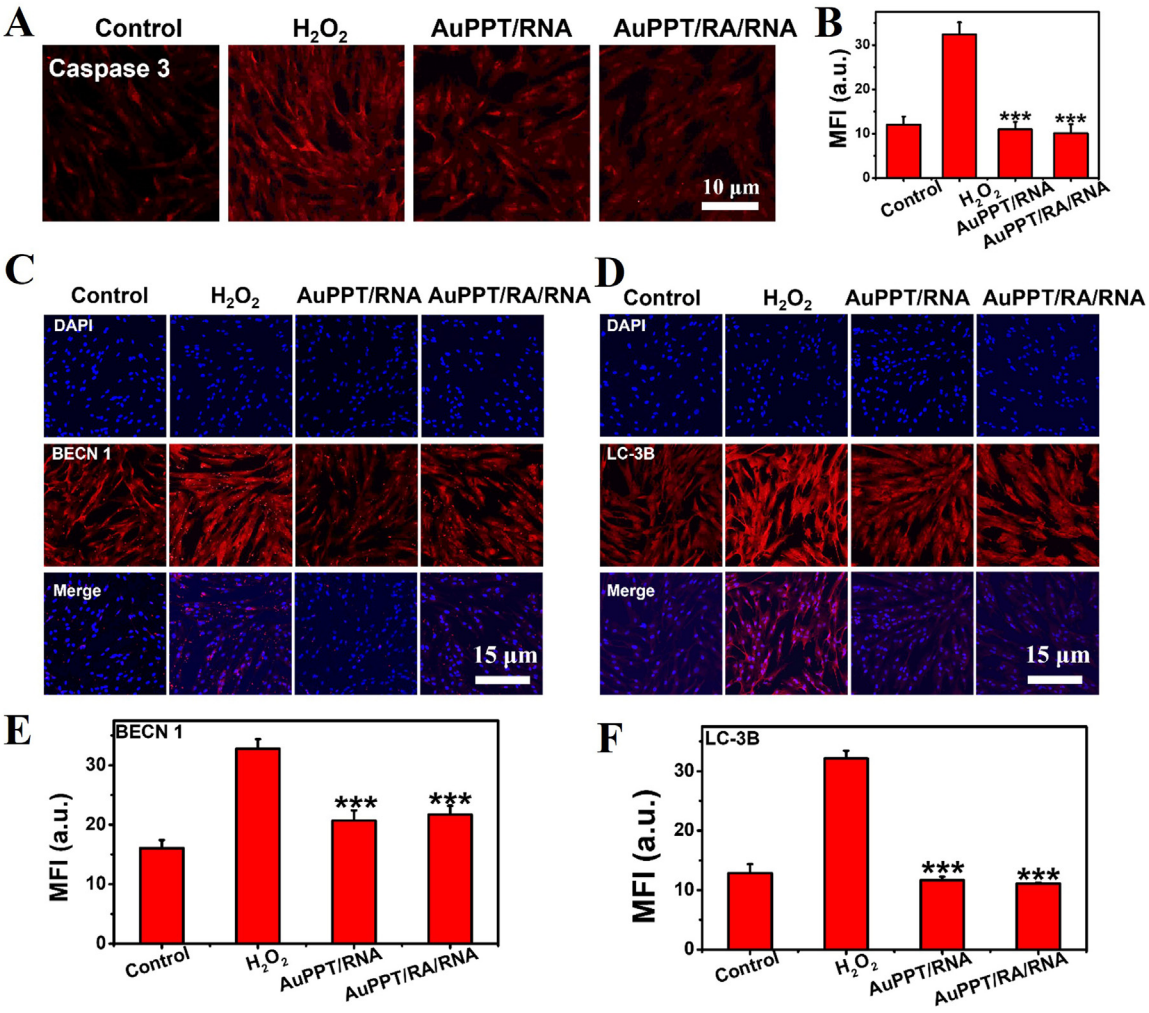

Fig. 6 – (A) Immunofluorescence staining images of Caspase 3 within MSCs in different groups and (B) corresponding fluorescence intensity, ***$P < 0.001$ compared with H_2O_2 group. Mean ± SD, $n = 3$. Representative immunostaining images of (C) BECN1 (red) and (D) LC-3B (red) of MSCs in different groups, the nuclei were stained by DAPI (blue). Quantification of fluorescence of (E) BECN1 and (F) LC-3B in different groups, ***$P < 0.001$ compared with H_2O_2 group. Mean ± SD, $n = 3$.

a sharp decline at 3 d post-transplantation, and almost disappeared in the following 2 d (Day 5), indicating the rapid death of the transplanted MSCs within 3 to 5 d, which was in accordance with the phenomenon reported in literature [40]. It is noteworthy that the BL signals in the AuPPT/RA/RNA group disappeared completely on Day 11 after transplantation, evidently manifesting that the co-delivery of RA and miRNA delayed the death of the transplanted MSCs to a certain extent (Fig. 7F). At the same time, the BL imaging signal of the unlabeled MSCs was detected for 5 d, inconsistent with the signal detection time of the AuPPT-labeled MSCs, illustrating that AuPPT labeling could not prolong the survival time of MSCs after transplantation (Fig. S11). Consequently, AuPPT/RA/RNA NPs labeling could not only monitor the distribution, migration, and location of the MSCs after transplantation by CT imaging but also lengthened the survival time of the transplanted MSCs through co-delivery of RA and miRNA into the cells.

In order to detect the *in vivo* metabolism of AuPPT and AuPPT/RA/RNA NPs, the lung frozen sections of the BLM mice after transplantation were imaged at Day 5 in the RBITC-AuPPT NPs labeled group and at Day 11 in the RBITC-AuPPT/RA/RNA labeled group, respectively. The results showed that the RBITC labeled NPs (red) were mainly distributed inside living MSCs (green), while some NPs escaped from MSCs, which may be due to the release of NPs caused by cell death (Fig. S12). On the one hand, most NPs were maintained in living cells, thus generating *in vivo* CT and BL signals. On the other hand, cell death caused the NPs to be released by MSCs and metabolized by the body, further explaining the gradual weakening of CT and BL signals *in vivo*.

3.7. *Therapeutic effect of the labeled* MSCs in vivo

To assess the therapeutic effect of the labeled MSCs *in vivo*, the AuPPT/RA/RNA or AuPPT labeled MSCs were administered

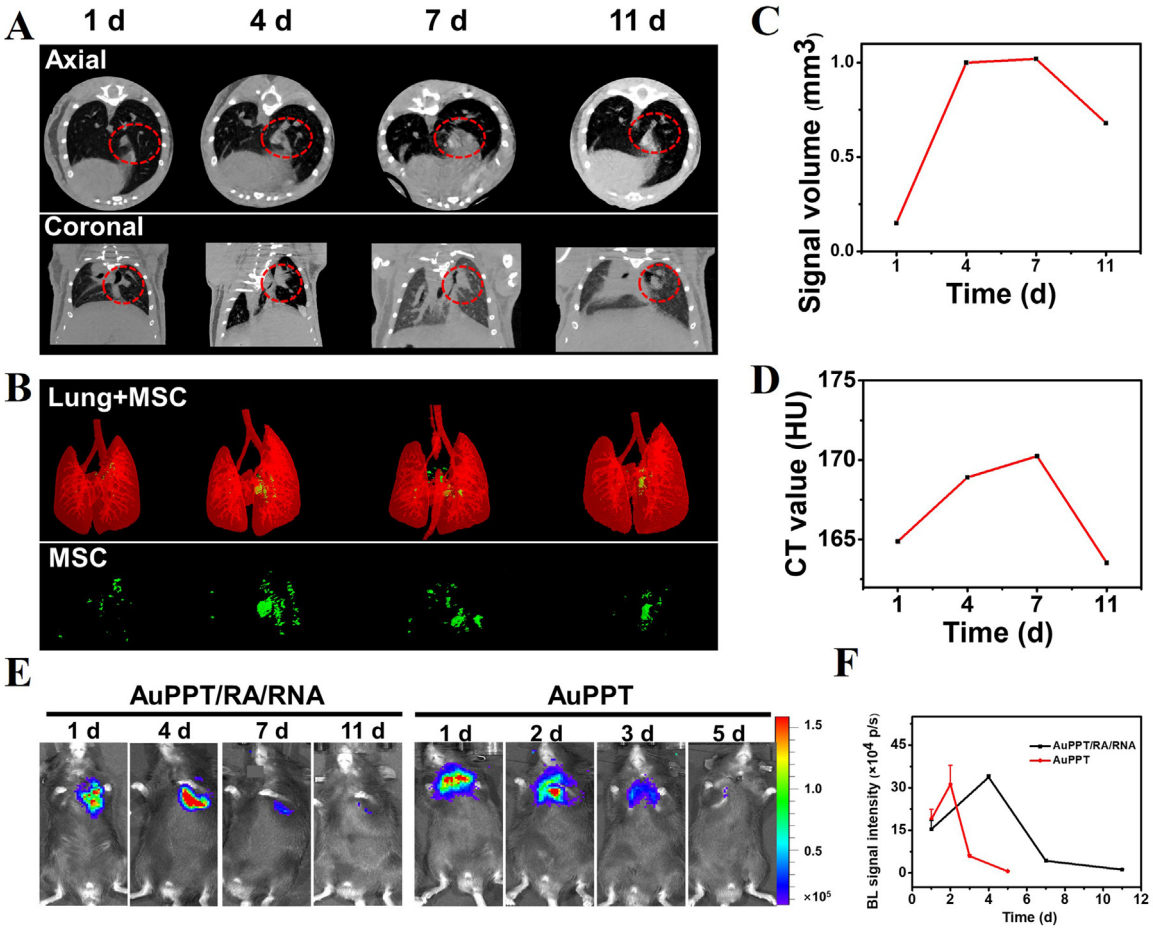

Fig. 7 – (A) CT images of the lung of IPF mouse after transplantation of the AuPPT/RA/RNA labeled MSCs at different time intervals. Axial section (top row) and corresponding coronal section (bottom row) were captured at various time points. (B) 3D reconstruction of the labeled MSCs at different time points after injection (red: lung, green: the transplanted MSCs). (C) CT signal volume and (D) mean CT value of the transplanted MSCs in lung tissue at different time points. (E) BL images of the IPF model mouse after transplantation of the AuPPT or AuPPT/RA/RNA labeled MSCs at different time points, and (F) corresponding quantitative statistics of signal intensity. Mean ± SD, $n = 5$.

into IPF mice after 3 d induction by BLM (named as AuPPT/RA/RNA and AuPPT groups, respectively), followed by CT imaging and histopathological test to diagnose the progression of pulmonary fibrosis in mice. The healthy mice injected with normal saline were used as a control group. CT diagnosis results presented that the lung tissue of the IPF mice in the BLM group exhibited obvious reticular shadow and interstitial thickening, covering almost the whole lung, in comparison to the control group (Fig. 8A, first row). While, an obviously decrease in the reticular shadow and interstitial area appeared after the injection of the MSCs labeled with AuPPT NPs, which was mainly due to the transplanted MSCs alleviating the progress of pulmonary fibrosis. Significantly, there was no obvious change in the lung tissue of the mice from the AuPPT/RA/RNA group, compared with the control group. CT imaging analysis is the predominant method to assess lung aeration status by identifying reticular and cellular cysts distributed in the double basal arteries and sub-pleura, reflecting the severity of pulmonary fibrosis [41]. This algorithm uses HU ranging from −434 to −121 and −120 to 120 to delineate poorly aerated and unaerated regions, respectively. As depicted in Fig. 8A and B, the nonaerated area (blue) was distinctly increased in the BLM group relative to the control group, but greatly decreased after the injection of the AuPPT or AuPPT/RA/RNA labeled MSCs. Noteworthy, in the AuPPT/RA/RNA group, the fully ventilated area (red) was much greater than that in the AuPPT group, indicating the optimal treatment effect of the AuPPT/RA/RNA labeled MSCs (Fig. 8A and B). After that, histopathological evaluation of the lung structure was performed by Hematoxylin and Eosin (H&E) staining as well as Masson trichromatic staining (Fig. 8C). H&E staining showed the injection of the labeled MSCs largely ameliorated interstitial deposition and alveolar septum thickened induced by pulmonary fibrosis. And the AuPPT/RA/RNA-labeled MSCs displayed better therapeutic outcome than the AuPPT-labeled MSCs. Besides, obviously inhibited collagen deposition was also observed in the AuPPT/RA/RNA group after Masson staining in contrast with the BLM and AuPPT groups.

Transforming growth factor-β (TGF-β) plays a pivotal role as a pro-fibrosis cytokine that facilitates the deposition of extracellular matrix, while α-smooth muscle actin (α-SMA)

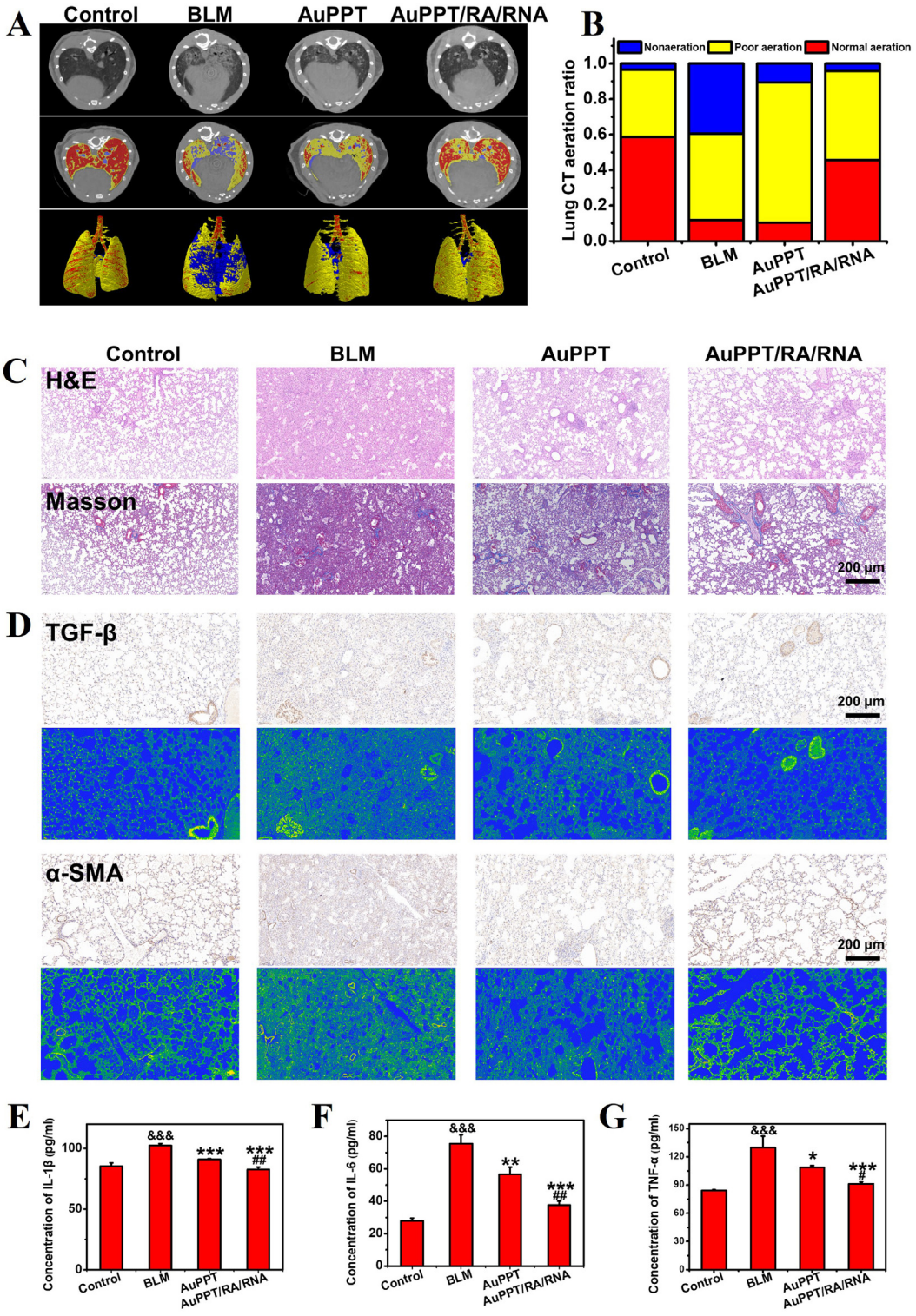

Fig. 8 – (A) Representative CT images of axial section and relevant 3D reconstruction images of the lung on Day 11 in different groups. (B) Percentages of pulmonary CT aerated ratio in different groups at 11 d post-transplantation (Blue: nonaerated region; yellow: poor aeration; red: normal aeration). (C) H&E and Masson trichromatic staining of lung sections in different groups. (D) Immunohistochemistry of TGF-β and α-SMA and corresponding gradient plots (Blue: cavity; Green: TGF-β or α-SMA factor) from each group. Inflammatory cytokine levels of (E) IL-1β, (F) IL-6, and (G) TNF-α in different groups. $^{\&\&\&}P < 0.001$ compared with Control group. $^{*}P < 0.05$ compared with BLM group. $^{**}P < 0.01$ compared with BLM group. $^{***}P < 0.001$ compared with BLM group. $^{\#}P < 0.05$ compared with AuPPT group. $^{\#\#}P < 0.01$ compared with AuPPT group. Mean ± SD, $n = 5$.

serves as an indicator of the advancement of pulmonary fibrosis [42]. The immunohistochemistry staining (brown signal) and corresponding gradient plots (green signal) of α-SMA and TGF-β showed that compared to the BLM and AuPPT groups, the expression of the fibrosis factors was apparently downregulated by the injection of the AuPPT/RA/RNA labeled MSCs (Fig. 8D).

Pulmonary fibrosis is often accompanied by the inflammatory process and produces numerous inflammatory factors, such as IL-6, IL-1β, and TNF-α, which can be detected by ELISA. The results in Fig. 8E-G reflected that the expression of pro-inflammatory cytokines (TNF-α, IL-6 and IL-1β) of IPF mice was significantly inhibited by both the AuPPT labeled and AuPPT/RA/RNA labeled MSCs, and the AuPPT/RA/RNA labeled MSCs performed better, further verifying the effectiveness of MSCs combined with drug co-delivery.

Overall, the AuPPT/RA/RNA labeled MSCs exhibited better therapeutic efficacy than the AuPPT-labeled MSCs, including the improvement in lung aeration, the reduction of inflammation cytokines and fibrosis factors, and the mitigation of fibrosis-caused histopathological damage, which mainly attributed to the fact that the drug delivery ameliorated the survival state of the transplanted MSCs. Briefly, after the co-delivery of RA and miRNA into MSCs by AuPPT NPs, RA regulated the internal mechanism of apoptosis, that is, by increasing the expression of SOD enzyme to rid high concentration of ROS in cells, while miRNA regulated the external mechanism of cell death by inhibiting the apoptosis and autophagy of the transplanted MSCs, thereby increasing cell viability. As a consequence, the AuPPT/RA/RNA-labeled MSCs showed a better therapeutic effect than the AuPPT-labeled MSCs by improving the survival rate of the transplanted MSCs.

Additionally, H&E staining of vital organs (heart, liver, spleen, lung, and kidney) revealed that AuPPT/RA/RNA NPs injection did not change the morphology of major organs, indicating their safety during the cell tracing and therapeutic process (Fig. S13).

4. Conclusion

In this study, a bifunctional Au-based system (AuPPT NPs) was constructed for effective drug delivery and CT imaging tracing of MSCs during the treatment of IPF. The positively charged AuPPT NPs had high nucleic acid (miRNA) and chemical drug (RA) loading and delivery abilities to remove the intracellular excess ROS and silence Caspase 3 expression, thereby improving the cell survival and therapeutic effect of transplanted MSCs. At the same time, benefiting from the exceptional cellular uptake ability of AuPPT NPs, the transplanted MSCs post-labeling with AuPPT enabled effective monitoring via CT imaging, which facilitated the acquisition of insights into distribution, migration, precise localization of MSCs *in vivo* during IPF treatment. In brief, the bifunctional AuPPT NPs exhibit a significant potential for clinical MSC-based IPF therapy.

Declaration of competing interest

The authors declare no conflicts of interest.

CRediT authorship contribution statement

Xiaodi Li: Writing – review & editing, Writing – original draft, Validation, Project administration, Methodology, Investigation, Formal analysis, Data curation, Conceptualization. **Shengnan Cheng:** Validation, Methodology. **Chenggong Yu:** Methodology, Conceptualization. **Yuxuan Li:** Methodology, Investigation. **Xiaoling Cao:** Methodology. **Yuhan Wang:** Methodology. **Zhijun Zhang:** Conceptualization. **Jie Huang:** Writing – review & editing, Validation, Supervision, Investigation, Funding acquisition, Conceptualization.

Acknowledgements

This work was supported by the National Natural Science Foundation of China (Grant No. 32171367), Natural Science Foundation of Jiangsu Province (Grant No. BK20230236), Science and Technology Project of Suzhou (Grant No. SS202135), and CAS-VPST Silk Road Science Fund 2021 (Grant No. 121E32KYSB20200021).

Supplementary materials

Supplementary material associated with this article can be found, in the online version, at doi:10.1016/j.ajps.2024.100944.

References

[1] Raghu G, Collard HR, Egan JJ, Martinez FJ, Behr J, Brown KK, et al. An official ATS/ERS/JRS/ALAT statement: idiopathic pulmonary fibrosis: evidence-based guidelines for diagnosis and management. Am J Respir Crit Care Med 2011;183(6):788–824.
[2] Ionescu LI, Alphonse RS, Arizmendi N, Morgan B, Abel M, Eaton M, et al. Airway delivery of soluble factors from plastic-adherent bone marrow cells prevents murine asthma. Am J Respir Cell Mol Biol 2012;46(2):207–16.
[3] Li L, Chen X, Wang WE, Zeng C. How to improve the survival of transplanted mesenchymal stem cell in ischemic heart? Stem Cells Int 2016;2016:9682757.
[4] Telukuntla KS, Suncion VY, Schulman IH, Hare JM. The advancing field of cell-based therapy: insights and lessons from clinical trials. J Am Heart Assoc 2013;2(5):e000338.
[5] Song H, Cha MJ, Song BW, Kim IK, Chang W, Lim S, et al. Reactive oxygen species inhibit adhesion of mesenchymal stem cells implanted into ischemic myocardium via interference of focal adhesion complex. Stem Cells 2010;28(3):555–63.
[6] Danial NN, Korsmeyer SJ. Cell death: critical control points. Cell 2004;116(2):205–19.
[7] Ahlemeyer B, Krieglstein J. Retinoic acid reduces staurosporine-induced apoptotic damage in chick embryonic

neurons by suppressing reactive oxygen species production. Neurosci Lett 1998;246(2):93–6.
[8] Ahlemeyer B, Krieglstein J. Inhibition of glutathione depletion by retinoic acid and tocopherol protects cultured neurons from staurosporine-induced oxidative stress and apoptosis. Neurochem Int 2000;36(1):1–5.
[9] Boatright KM, Salvesen GS. Mechanisms of caspase activation. Curr Opin Cell Biol 2003;15(6):725–31.
[10] Panasiewicz G, Majewska M, Szafrańska B. The involvement of luteinizing hormone (LH) and pregnancy-associated glycoprotein family (PAG) in pregnancy maintenance in the pig. Reprod Biol 2004;4(2):143–63.
[11] Huntzinger E, Izaurralde E. Gene silencing by microRNAs: contributions of translational repression and mRNA decay. Nat Rev Genet 2011;12(2):99–110.
[12] Li J, Yuan J. Caspases in apoptosis and beyond. Oncogene 2008;27(48):6194–206.
[13] Ham O, Lee SY, Lee CY, Park JH, Lee J, Seo HH, et al. Let-7b suppresses apoptosis and autophagy of human mesenchymal stem cells transplanted into ischemia/reperfusion injured heart 7by targeting caspase-3. Stem Cell Res Ther 2015;6(1):147.
[14] Li X, Li Y, Yu C, Bao H, Cheng S, Huang J, et al. ROS-responsive Janus Au/mesoporous silica core/shell nanoparticles for drug delivery and long-term CT imaging tracking of MSCs in pulmonary fibrosis treatment. ACS Nano 2023;17(7):6387–99.
[15] Oliveira FA, Nucci MP, Filgueiras IS, Ferreira JM, Nucci LP, Mamani JB, et al. Noninvasive tracking of hematopoietic stem cells in a bone marrow transplant model. Cells 2020;9(4):939.
[16] Acharya D, Park J, Lee Y, Hamm IS, Lee DS, Moon SS, et al. Clinical characteristics of the COVID-19 patients with pneumonia detected by computerized tomography but negative for infiltration by X-ray. Healthcare 2020;8(4):518.
[17] Meng X, Wu Y, Bu W. Functional CT contrast nanoagents for the tumor microenvironment. Adv Healthcare Mater 2021;10(5):2000912.
[18] Yu C, Chen Z, Li X, Bao H, Wang Y, Zhang B, et al. pH-triggered aggregation of gold nanoparticles for enhanced labeling and long-term CT imaging tracking of stem cells in pulmonary fibrosis treatment. Small 2021;17(33):e2101861.
[19] Huang J, Bao H, Li X, Zhang Z. *In vivo* CT imaging tracking of stem cells labeled with Au nanoparticles. View 2021;3(3):20200119.
[20] Lv Y, Yu C, Li X, Bao H, Song S, Cao X, et al. ROS-activatable nanocomposites for CT imaging tracking and antioxidative protection of mesenchymal stem cells in idiopathic pulmonary fibrosis therapy. J Control Release 2023;357:249–63.
[21] Yu C, Lv Y, Li X, Bao H, Cao X, Huang J, et al. SOD-Functionalized gold nanoparticles as ROS scavenger and CT contrast agent for protection and imaging tracking of mesenchymal stem cells in idiopathic pulmonary fibrosis treatment. Chem Eng J 2023;459:141603.
[22] Han X, Li Y, Xu Y, Zhao X, Zhang Y, Yang X, et al. Reversal of pancreatic desmoplasia by re-educating stellate cells with a tumor microenvironment-activated nanosystem. Nat Commu 2018;9(1):3390.
[23] Bao H, Xia Y, Yu C, Ning X, Liu X, Fu H, et al. CT/bioluminescence dual-modal imaging tracking of mesenchymal stem cells in pulmonary fibrosis. Small 2019;15(46):e1904314.
[24] Li X, Yu C, Bao H, Chen Z, Liu X, Huang J, et al. CT/bioluminescence dual-modal imaging tracking of stem cells labeled with Au@PEI@PEG nanotracers and RfLuc in nintedanib-assisted pulmonary fibrosis therapy. Nanomedicine:NBM 2022;41:102517.
[25] Brooks H, Lebleu B, Vivès E. Tat peptide-mediated cellular delivery: back to basics. Adv Drug Deliv Rev 2005;57(4):559–77.
[26] Wu S, Yang C, Yan X. A dual-functional persistently luminescent nanocomposite enables engineering of mesenchymal stem cells for homing and gene therapy of glioblastoma. Adv Funct Mater 2017;27(11):1604992.
[27] Zhdanov RI, Podobed OV, Vlassov VV. Cationic lipid-DNA complexes-lipoplexes-for gene transfer and therapy. Bioelectrochemistry 2002;58(1):53–64.
[28] Kadam R, Ghawali J, Waespy M, Maas M, Rezwan K. Janus nanoparticles designed for extended cell surface attachment. Nanoscale 2020;12(36):18938–49.
[29] Muthuselvi C, Pandiarajan SS, Ravikumar B, Athimoolam S, Srinivasan N, Krishnakumar RV. FT-IR and FT-Raman spectroscopic analyzes of indeno quinoxaline derivative crystal. Asian J Applied Sci 2018;11(2):83–91.
[30] Gooding M, Browne LP, Quinteiro FM, Selwood DL. siRNA delivery: from lipids to cell-penetrating peptides and their mimics. Chem Biol Drug Des 2012;80(6):787–809.
[31] Kosuge M, Takeuchi T, Nakase I, Jones AT, Futaki S. Cellular internalization and distribution of arginine-rich peptides as a function of extracellular peptide concentration, serum, and plasma membrane associated proteoglycans. Bioconjug Chem 2008;19(3):656–64.
[32] Astolfo A, Arfelli F, Schültke E, James S, Mancini L, Menk RH. A detailed study of gold-nanoparticle loaded cells using X-ray based techniques for cell-tracking applications with single-cell sensitivity. Nanoscale 2013;5(8):3337–45.
[33] Teixeira CC, Shapiro IM, Hatori M, Rajpurohit R, Koch C. Acid modulation of glutathione and cysteine metabolism in chondrocytes. Biochem J 1996;314(Pt 1):21–6.
[34] Choudhary R, Baker KM, Pan J. All-trans retinoic acid prevents angiotensin II- and mechanical stretch-induced reactive oxygen species generation and cardiomyocyte apoptosis. J Cel Physiol 2008;215(1):172–81.
[35] Ricci JE, Gottlieb RA, Green DR. Caspase-mediated loss of mitochondrial function and generation of reactive oxygen species during apoptosis. J Cell Biol 2003;160(1):65–75.
[36] Portt L, Norman G, Clapp C, Greenwood M, Greenwood MT. Anti-apoptosis and cell survival: a review. Biochim Biophys Acta 2011;1813(1):238–59.
[37] Zhang Y, Ren J. Targeting autophagy for the therapeutic application of histone deacetylase inhibitors in ischemia/reperfusion heart injury. Circulation 2014;129(10):1088–91.
[38] Mariño G, Niso-Santano M, Baehrecke EH, Kroemer G. Self-consumption: the interplay of autophagy and apoptosis. Nat Rev Mol Cell Bio 2014;15(2):81–94.
[39] Matsui Y, Takagi H, Qu X, Abdellatif M, Sakoda H, Asano T, et al. Distinct roles of autophagy in the heart during ischemia and reperfusion: roles of AMP-activated protein kinase and Beclin 1 in mediating autophagy. Circ Res 2007;100(6):914–22.
[40] Yang YJ, Qian HY, Huang J, Geng YJ, Gao RL, Dou KF, et al. Atorvastatin treatment improves survival and effects of implanted mesenchymal stem cells in post-infarct swine hearts. Eur Heart J 2008;29(12):1578–90.
[41] Cocconcelli E, Balestro E, Biondini D, Barbiero G, Polverosi R, Calabrese F, et al. High-resolution computed tomography (HRCT) reflects disease progression in patients with idiopathic pulmonary fibrosis (IPF): relationship with lung pathology. J Clin Med 2019;8(3):399.
[42] Li H, Zhao C, Tian Y, Lu J, Zhang G, Liang S, et al. Src family kinases and pulmonary fibrosis: a review. Biomed Pharmacother 2020;127:110183.